A NOVEL ROBOT PATH PLANNING ALGORITHM BASED ON THE IMPROVED WILD HORSE OPTIMISER WITH HYBRID STRATEGIES

Juntao Zhao*,** Xiaochuan Luo,* and Yong Li*

Abstract

Metaheuristic algorithms play a pivotal role in addressing the challenges of robot path planning, offering versatile, and efficient solutions. Nevertheless, the standard wild horse optimiser (WHO) has limitations, including limited population diversity during initialisation, constrained global search capability, and challenges in escaping local optima. This paper proposed an improved WHO with hybrid strategies (HI-WHO) to overcome these disadvantages in solving robot path planning problem. The algorithm employs Sobol sequence for uniform population initialisation, integrating the Lévy flight strategy, and dynamic adaptive factor to balance exploration and exploitation. Concurrently, it ensures global search capability and prevents local optima by using the lens imaging opposition-based learning strategy and greedy mechanism. The robustness and effectiveness of the enhanced algorithm were evaluated on a set of 20 benchmark functions. Finally, the improved algorithm, combined with the cubic B-Spline interpolation method, addresses robot path planning in grid map environments, demonstrating its exceptional stability and optimal performance.

Key Words

Wild horse optimiser (WHO), Sobol sequence, Lévy flight, dynamic self-adaptive factor, opposition-based learning, cubic B-Spline, path planning

1. Introduction

Recently, rapid advances in robot technology have led to a significant increase in the demand for autonomous robots. Path planning, a crucial element of autonomous systems, has drawn considerable interest from researchers [1]. It aims to find the most efficient trajectory from an initial position to a specified destination within a given environment. This trajectory should minimise both travel time and distance while guaranteeing collision avoidance with obstacles and adherence to defined constraints [2]–[4].

Path planning is a challenging NP-hard problem. The methods can be categorised into two types: classical and metaheuristic [5]. Classical algorithms, such as gradient descent (GD), cell decomposition (CD), and artificial potential field (APF) often suffer from problems like getting stuck to a local optimum, slow convergence speed, and low solution quality, significantly affecting the accuracy and efficiency. It is worth noting that these methods often rely on having comprehensive prior knowledge of the environment to establish a viable path between the starting and destination points. Therefore, researchers have proposed various metaheuristic algorithms, such as particle swarm optimisation (PSO) [6], artificial bee colony (ABC) [7], Harris Hawks optimisation (HHO) [8], and sparrow search algorithm (SSA) [9], which have been applied to solve robot path planning problems. These approaches excel at navigating unknown or partially known environments by iteratively generating temporary paths, advancing step by step toward the destination, and selecting the best path based on fitness. Additionally, metaheuristic algorithms offer advantages, such as few adjustable parameters, no gradient mechanisms, strong parallelism, and ease of interpretation and understanding.

The wild horse optimiser (WHO) is a newly developed metaheuristic algorithm demonstrating remarkable performance in solving complex optimisation problems [10]. Nonetheless, WHO still exhibits limitations, including insufficient population diversity during initialisation, limited global search capabilities, challenges in escaping local optima in later stage, and difficulties in effectively leveraging individual information to achieve better results [11]. This paper proposes a novel robot path planning algorithm based on the improved WHO with hybrid strategies (HI-WHO), intending to overcome the limitations of the standard WHO and further enhance its performance and

* College of Information Science and Engineering, Northeastern University, Shenyang, China 110819; e-mail: zhaojuntao@stumail.neu.edu.cn; luoxch@mail.neu.edu.cn

** EPROAD EA 4669, University of Picardy Jules Verne, Amiens, France 80000; e-mail: 1776733509@qq.com

Corresponding authors: Juntao Zhao and Xiaochuan Luo

Recommended by Hao Zhang

(DOI: 10.2316/J.2024.206-1087)

applicability. The effectiveness of the improved algorithm is verified through experiments conducted in simple and complex grid map environments. Hence, the contributions of this research can be summarised as follows:

- The proposed HI-WHO integrates hybrid strategies, leading to superior global search capability, faster convergence, improved accuracy, and the ability to escape local optima.
- Developing a mathematical model for robot path planning and employing HI-WHO with cubic B-Spline curves to generate optimised and smooth path.
- Broaden the practical utility of WHO by showcasing its effectiveness in solving robot path planning problem.

The remaining sections are organised as follows: Section 2 focuses on modelling robot path planning problem and introduces the principles of cubic B-Spline curve-based path smoothing. Section 3 presents an overview of the standard WHO. Section 4 describes the implementation of the enhanced WHO with hybrid strategies. In Section 5, the improved algorithm is evaluated using 20 different types of benchmark functions. Section 6 presents the results and discussions of HI-WHO applied in robot path planning. Finally, Section 7 concludes the study and suggests future directions for research.

2. Problem Statement of Mobile Robot Path Planning

This section provides an overview of the robot path planning problem. It begins by exploring the grid map environment modelling process. Next, it delves into establishing the objective function that quantitatively evaluates the optimal path. Finally, it introduces path smoothing techniques to enhance the smoothness and continuity of the trajectory.

2.1 Grid Map Environment Modelling

This study utilises HI-WHO to address the global path planning problem within a two-dimensional environment featuring finite static obstacles, which has applications in practical scenarios like unmanned workshops, intelligent warehouses, and specialised environments [12], [13]. Standard modelling methods, including octree, grid, topology, and accessible space, are traditionally employed [14]. Among them, the grid method is a widely accepted and straightforward approach, which simplifies the environment model while delivering satisfactory results. Thus, this study adopts the grid-based approach, as depicted in Fig. 1.

In Fig. 1, the black regions indicate obstacles, while the white regions represent the navigable area. The robot can move in eight neighbouring directions from its central position. The objective is to navigate from the starting point indicated by the circle to the destination represented by the star. The environment map, denoted as G, can be represented by an $N \times N$ binary matrix, where 0 denotes the navigable region, and 1 denotes the static obstacle [15]. Additionally, each grid in the map is sequentially numbered as $\{1, 2 \ldots, N \times N\}$. The centre coordinates $(x,\ y)$ of any

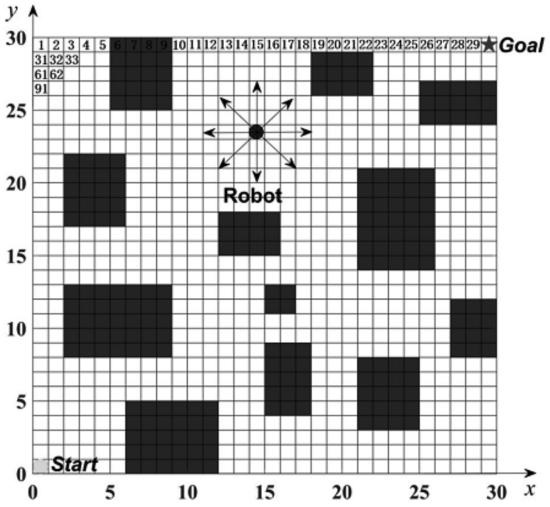

Figure 1. Grid map model.

grid n can be calculated using (1) and (2).

$$x = \begin{cases} n\%N - 0.5, n\%N \neq 0 \\ N - 0.5, n\%N = 0 \end{cases} \tag{1}$$

$$y = \begin{cases} N - 0.5 - \left\lfloor \frac{n}{N} \right\rfloor, n\%N \neq 0 \\ N + 0.5 - \left\lfloor \frac{n}{N} \right\rfloor, n\%N = 0 \end{cases} \tag{2}$$

In which % denotes the modulo operation, and $\lfloor\rfloor$ represents the floor function.

2.2 Establishment of Objective Function

The objective function aims to determine the optimal solution by evaluating the fitness value. When conducting path planning in a two-dimensional grid map, the following conditions must be met:

- The path must be confined within the boundaries of the map, ensuring that the path does not extend beyond the map edges.
- The length of the planned path should be minimised, aiming to achieve an optimal path for the robot.
- The path should avoid traversing through areas occupied by obstacles, preventing collisions during the robot's movement.

Under the given constraints, the robot aims to plan an optimal collision-free path from the starting point $S(x_s, y_s)$ to the target point $E(x_e, y_e)$ within the predefined grid map. The intermediate points can be denoted as $P_i \in \{(x_i, y_i)\},\ i = 1,\ \ldots,\ n$. Therefore, the generated path can be represented as a sequence comprising the starting, target, and intermediate path points, *i.e.*, $\{S, P^1, P^2, \ldots, P^n, E\}$. Finally, the path can be obtained by sequentially connecting these points.

Based on the analysis, robot path planning can be formulated as a single-objective optimisation problem, aiming to minimise the fitness value. Considering the constraints mentioned above, the objective function is

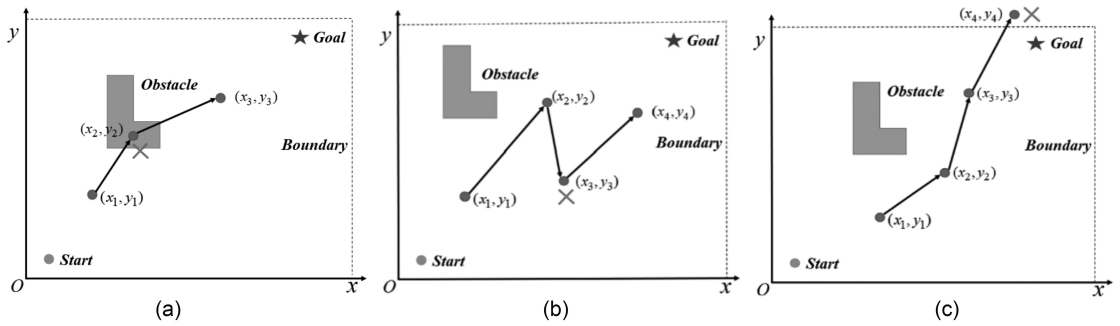

Figure 2. Three kinds of invalid path points: (a) $(x_i, y_i) \in$ obstacle; (b) $x_{i+1} < x_i \parallel y_{i+1} < y_i$; and (c) $x_i < x_{\min} \parallel x_i > x_{\max} \parallel y_i < y\min \parallel yi > y\max$.

expressed by (3).

$$\text{Minimize } F = \sum_{i=1}^{n} D_i + O(P_i) \times M. \tag{3}$$

$$\text{Subject to } \begin{cases} x_{\min} \leq x_i \leq x_{\max} \\ y_{\min} \leq y_i \leq y_{\max} \end{cases}$$

where D_i represents the path length at the i-th iteration, calculated using Euclidean distance, as (4). $O(P_i)$ denotes the penalty value for point P_i. If the point intersects with an obstacle, exhibits a reversal, or exceeds the boundaries, it is considered an invalid path point, as depicted in Fig. 2. In such cases, the penalty value is $N \times N$. Otherwise, it is set to 0. The specific definition is given by (5). M represents the number of invalid points.

$$D_i = \sqrt{(x_{i+1} - x_i)^2 + (y_{i+1} - y_i)^2} \tag{4}$$

$$O(P_i) = \begin{cases} 0, & P_i \in \text{allowed}_p \\ N \times N, & \text{otherwise} \end{cases} \tag{5}$$

2.3 Path Smoothing

Path smoothing is crucial in optimising the suitability of the generated path. This step focuses on eliminating sharp curves and applying cubic B-Spline curve interpolation to refine the path.

First, the slope between a point P_i and its adjacent points P_{i-1} and P_{i+1} is computed. If the path between these points is not horizontal or vertical, it indicates the presence of a turning point that requires smoothing. Next, the coordinates of the adjacent points to the turning point are calculated, and their existence in the grid-based map G is checked for obstacles. The turning point is considered redundant and can be removed if no obstacles are found. This process is repeated until all redundant turning points in the path are eliminated.

Finally, the processed path is smoothed using B-Spline curves, which possess advantages, such as geometric invariance, convex hull property, convexity preservation, and local support [16], [17]. The smoothing effect of using cubic B-spline curve is illustrated in Fig. 3.

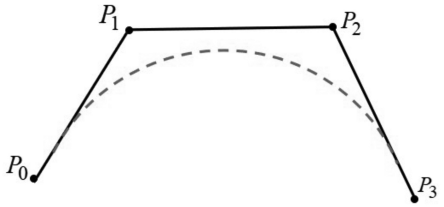

Figure 3. Smoothing effect of using cubic B-spline curve.

3. Standard Wild Horse Optimiser

The WHO is an innovative optimisation algorithm that emulates the life behaviour of a wild horse herd in non-territorial regions [10]. The possesses distinct characteristics across five aspects.

3.1 Population Initialisation and Group Formation

WHO initialises the population by generating random individuals within the search space. Then, the initial population is divided into several groups using (6), and the leaders $N_{Stallion}$ is determined by the number of stallion groups, denoted as G. The remaining horse groups, including mares and foals, are evenly distributed with $N_{Foal} = N - G$, where N denotes the population size.

$$G = \lceil N \times PS \rceil \tag{6}$$

where PS represents the percentage of stallion groups partitioned from the initial population.

3.2 Grazing Behaviour

The foals spend most of their time grazing around the group. The algorithm simulates this behaviour using (7), where the position of the stallion is considered as the centre of the grazing area, and the other members (mares and foals) graze around the centre. They move and search around the leader within different radii.

$$\overline{X}_{i,G}^{j} = 2Z\cos(2\pi \text{RZ}) \times (X_{\text{Stallion}}^{j} - X_{i,G}^{j}) + X_{\text{Stallion}}^{j} \tag{7}$$

where X_{Stallion}^{j} represents the position of the stallion (leader), $X_{i,G}^{j}$ represents the current position of the group member (mare or foal), Z is an adaptive parameter

calculated using (8), and R is a uniform random number ranging from -2 to 2. The individuals can move within different radii by using the *cos* function. $\overline{X}^{j}_{i,G}$ denotes the updated position after the grazing behaviour.

$$\begin{cases} P = \overrightarrow{R}_1 < TDR \\ IDX = (P == 0) \\ Z = R_2 \Theta IDX + \overrightarrow{R}_3 \Theta(\sim \text{IDX}) \end{cases} \tag{8}$$

where P is a vector containing zeros and ones, $\overrightarrow{R}_1$and $\overrightarrow{R}_3$ are the random vectors with uniform distribution, and the values range from 0 to 1. R_2 is a uniform random number ranging from 0 to 1, IDX represents the index of elements in $\overrightarrow{R}_1$ that satisfy (P == 0), and TDR is an adaptive parameter. As the number of iterations increases, the value of TDR decreases from 1 to 0, which is calculated as:

$$TDR = 1 - \frac{t}{T_{\max}} \tag{9}$$

where t represents the current iteration number, and $T_{\max}$ is the maximum number of iterations.

3.3 Mating Behaviour

Upon reaching maturity, male and female foals from distinct groups can mate and produce offspring. These offspring must depart from their current group and join a different one. Equation (10) shows the mating behaviour using the mean crossover operator.

$$\begin{cases} X^{o}_{G,k} = \text{Crossover}(X^{p}_{G,i}, X^{q}_{G,j}); \\ i \neq j \neq k, o = p = \text{end}; \\ \text{Crossover} = \text{Mean}. \end{cases} \tag{10}$$

where $X^{o}_{G,k}$ represents the position of individual o in group k. It leaves group k and is replaced by offspring generated through mating between individuals p in group i ($X^{p}_{G,i}$) and q in group j ($X^{q}_{G,j}$).

3.4 Group Leadership

Group leaders lead their groups toward more suitable locations (watering hole). If the current group occupies a dominant position, they continue to use the area. However, if another group occupies the area, the leader needs to guide the current group away from that area. This process is expressed in (11) and (12).

$$\begin{aligned} \overline{X}^{i}_{\text{Stallion}} &= 2Z\cos(2\pi \text{RZ}) \times (WH - X^{i}_{\text{Stallion}}) \\ &\quad + WH, R_5 > 0.5 \end{aligned} \tag{11}$$

$$\begin{aligned} \overline{X}^{i}_{\text{Stallion}} &= Z\cos(2\pi \text{RZ}) \times (WH - X^{i}_{\text{Stallion}}) \\ &\quad - WH, R_5 \leq 0.5 \end{aligned} \tag{12}$$

where $\overline{X}^{i}_{\text{Stallion}}$ represents the next leader position in group i, WH denotes the position of the most suitable area, X^{i}_{Stallion} represents the current leader position in group i, R is a random number between -2 and 2, and π equals 3.14.

3.5 Leader Exchange and Selection

The leaders are randomly selected at the initial phase and updated based on the fitness values during the iterations. The leader's position is updated according to (13).

$$X^{i}_{\text{Stallion}} = \begin{cases} \overline{X}^{i}_{\text{Stallion}}, \text{cost}(\overline{X}^{i}_{\text{Stallion}}) < \text{cost}(X^{i}_{\text{Stallion}}) \\ X^{i}_{\text{Stallion}}, \text{cost}(\overline{X}^{i}_{\text{Stallion}}) > \text{cost}(X^{i}_{\text{Stallion}}) \end{cases} \tag{13}$$

4. Improved Wild Horse Optimiser with Hybrid Strategies (HI-WHO)

This chapter introduces the improved WHO with hybrid strategies (HI-WHO). It covers the use of the Sobol sequence for population initialisation, incorporates the Lévy flight strategy for individual position updates, and integrates a nonlinear dynamic self-adaptive factor along with the lens imaging opposition-based learning strategy to enhance capabilities. The chapter also offers insights into the implementation and flowchart of HI-WHO.

4.1 Sobol Sequence to Initialise Populations

The initial population's distribution significantly impacts the efficiency and accuracy of metaheuristic algorithms. A balanced distribution enhances search efficiency. Unlike the standard WHO's random approach, this paper employs low-discrepancy sequences, specifically the Sobol sequence, for initialising the population. This choice ensures an orderly distribution of the foal population around the leader horse, offering advantages, such as uniformity, efficient computation, and a broader sampling range [18], as shown in (14).

$$X_n = LB + S_n \cdot (UB - LB) \tag{14}$$

where n is an integer ranging from 1 to N, [LB, UB] represents the range of the solution, S_n is a Sobol sequence ranging from 0 to 1, and X_n represents the initial population generated using the Sobol sequence.

Suppose the population size is 100, and the lower and upper bounds are 0 and 1, respectively. Figure 4 compares the distribution of the initial population using pseudorandom numbers and the Sobol sequence. It can be observed that the population initialised using the Sobol sequence exhibits a more uniform distribution and covers a broader range compared to the population initialised using pseudorandom numbers. This step establishes a robust foundation for the global search algorithm.

4.2 Lévy Flight Strategy for Individual Position Update

The WHO's individual movement, involving foals and mares, centres on updating their positions primarily influenced by the group leader (stallion). In the standard WHO, the position update method for individuals with lower fitness values is limited, potentially causing stagnation. To address this, the Lévy flight strategy is introduced, inspired by the Cuckoo search (CS) algorithm

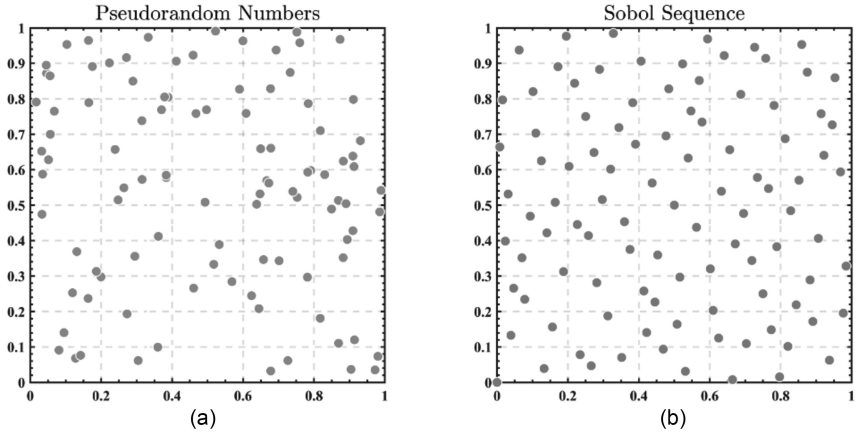

Figure 4. Different distributions of the initial population: (a) pseudorandom and (b) Sobol sequence.

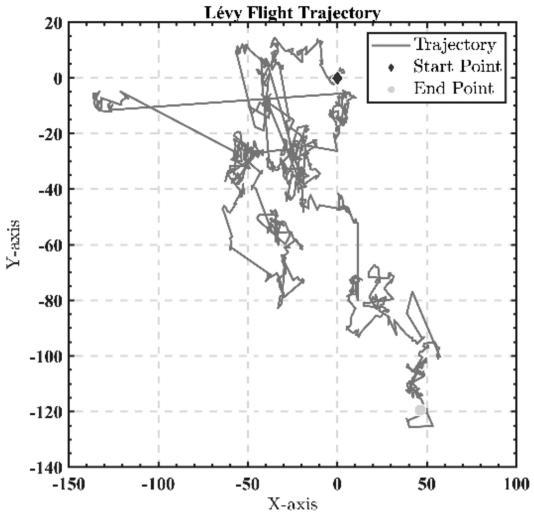

Figure 5. The trajectory of Lévy flight with 1,000 steps.

[19]. This strategy enhances population diversity, broadens the search scope, and facilitates escaping local optima.

The Lévy flight pattern is selected for its capacity to create random searches following the Lévy distribution. This distribution exhibits a walking pattern that combines shorter walks with higher probability and longer walks with lower probability. Integrating Lévy flight into the position update process prevents stagnation and being trapped in local optima by introducing randomness and exploration around the updated position. Figure 5 shows the trajectory of Lévy flight in a two-dimensional space, illustrating its ability to inject randomness into the search process and enhance effective exploration.

If a random value R_4 is below the mating probability threshold PC, the position update follows the mating behaviour method, as depicted in (10). Conversely, when R_4 exceeds PC, individuals undergo position updates using the Lévy flight strategy, as outlined in (15).

$$\overline{X}_{i,G}^{j} = \alpha(X_{\text{Stallion}}^{j} - Xa_{i,G}^{j}) \oplus Levy(\delta) + X_{\text{Stallion}}^{j}, R_4 > PC \tag{15}$$

where α is the step size adjustment coefficient with a value of 0.01, $\oplus$ denotes element-wise multiplication, and $Lévy(\delta)$ represents a path that follows the Lévy distribution. The Lévy distribution is defined as:

$$\text{Levy}(\delta) = \frac{\mu}{|\upsilon|^{\frac{1}{\delta}}} \tag{16}$$

where μ and ν follow normal distribution as described in (17) and (18):

$$\mu \sim N(0, \sigma_\mu^2), \upsilon \sim N(0, \sigma_v^2) \tag{17}$$

$$\sigma_\mu = \left[\frac{\Gamma(1+\delta)\sin(\delta\pi/2)}{\Gamma((1+\delta)/2)\delta 2^{(\delta-1)}}\right]^{1/\delta}, \sigma_v = 1 \tag{18}$$

where Γ represents the gamma function, and δ is a value ranging from 0 to 2. In this paper, we choose the value of $\delta = 1.5$.

4.3 Nonlinear Dynamic Self-Adaptive Factor

Equation (9) uses a linear factor to regulate variable Z in WHO, which is crucial for balancing between global exploration and local exploitation. This study introduces a dynamic nonlinear adaptive factor in (19), which adjusts its magnitude as iterations increase. Initially, it is set to a larger value, facilitating rapid descent for efficient global exploration. With progressing iterations, the adaptive factor gradually decreases, improving the algorithm's capacity for local search. The modification involves defining TDR as a nonlinear function of the current iteration number (t) at each time step. In the initial stage, TDR approaches a value close to 1, and as t approaches $T_{\max}$, it approaches a value close to 0. Between 0 and $T_{\max}$, TDR nonlinearly decreases with the increasing value of t.

$$TDR = \left[1 + \cos\left(\frac{\pi}{2} \cdot \frac{t}{T_{\max}} + \frac{\pi}{2}\right)\right]^{\text{dnw}} \tag{19}$$

where dnw denotes the dynamic nonlinear adjustment factor.

Figure 6 illustrates the relationship between dnw and TDR, showcasing how TDR changes with dnw ranging from 0.2 to 3.4. Notably, dnw significantly influences the

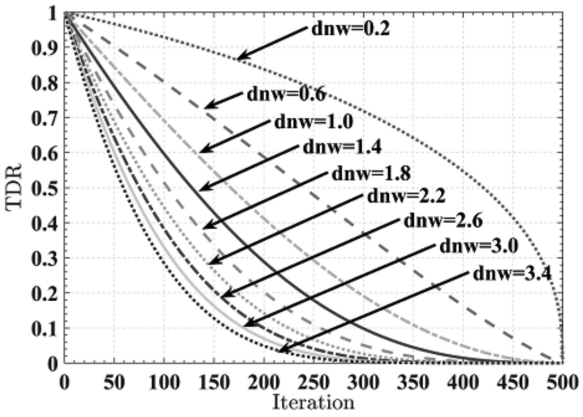

Figure 6. *TDR* curves with different *dnw* values.

TDR curve, resulting in distinct nonlinear patterns. Larger *dnw* values produce a more concave curve, enabling an initial rapid decline in *TDR*, indicating improved global search capability and efficiency. Subsequent iterations make the *TDR* curve smoother, facilitating finer local search, and enhanced precision. Through extensive testing, a *dnw* value of 2.0 is found to strike a favourable balance between global exploration and local exploitation in the algorithm.

4.4 Lens Imaging Opposition-Based Learning Strategy

Initially, the WHO disperses individual horses across the search space, demonstrating robust global exploration. However, as indicated by (11) and (12) with each iteration, these individuals gradually converge towards the optimal position under the influence of the group leader. Consequently, the population gathers in a smaller region, reducing its diversity. If the group leader aligns with a local optimum during this process, there is a risk of premature convergence and stagnation. This paper introduces the lens imaging opposition-based learning strategy [20], which expands the search space by generating the reverse solution of the current one, identifying better candidate solutions for the given problem. The specific process is as follows.

Suppose an individual P exists in the range [LB, UB] with a height of h, and its projection is denoted as X (representing the global optimal individual). Next, a convex lens with a focal length of f is placed at the base point O (the midpoint of LB and UB). After being refracted by the convex lens, the individual P generates an image P' with a height of h', and its projection is denoted as X'. This image P' represents the opposite individual obtained through the lens imaging opposition-based learning strategy from the global optimal individual X, as shown in Fig. 7. The relationship between X and its corresponding reverse individual X' can be obtained through the principle of convex lens imaging as (20).

$$\frac{(LB+UB)/2 - X}{X' - (LB+UB)/2} = \frac{h}{h'} \tag{20}$$

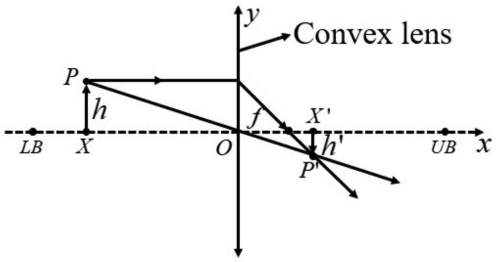

Figure 7. Illustration of lens imaging opposition-based learning strategy.

where $\lambda = h/h'$ is the scaling factor between the heights P and P'. The reverse individual X' can be obtained as follows.

$$X' = \frac{LB+UB}{2} + \frac{LB+UB}{2\cdot\lambda} - \frac{X}{\lambda} \tag{21}$$

This study adopts a dynamic nonlinear scaling factor, as shown in (22), which adjusts λ to obtain dynamically updated candidate solutions.

$$\lambda = \lambda_{\min} + (\lambda_{\max} - \lambda_{\min}) \cdot \left(1 - \frac{t}{T_{\max}}\right)^2 \tag{22}$$

where λ_{min} and $\lambda_{\max}$ represent the minimum and maximum scaling factors, respectively. If the search space is extended to high dimensions, the following equation can be obtained:

$$X'_{i,j} = \frac{LB_j + UB_j}{2} + \frac{LB_j + UB_j}{2\cdot\lambda} - \frac{X_{i,j}}{\lambda} \tag{23}$$

where $X_{i,j}$ represents the position of individual i on dimension j, $X'_{i,j}$ represents the reverse solution, and LB_j and UB_j represent the lower and upper bounds of the decision variable on dimension j.

Although applying the lens imaging opposition-based learning strategy can expand the search range and improve the ability to escape local optima, it is difficult to determine whether the generated opposite individuals are better than the current best. Therefore, this paper uses a greedy mechanism to further select the better individual based on the fitness value. This process can be represented by (24).

$$X_{\text{new}}(t) = \begin{cases} X, \text{cost}(X) < \text{cost}(X') \\ X', \text{cost}(X) \geq \text{cost}(X') \end{cases} \tag{24}$$

4.5 Implementation and Flowchart of the HI-WHO

The flowchart of HI-WHO is presented in Fig. 8. It takes population size, search space dimension, range, and maximum iterations as input and starts with the creation of foal groups using the Sobol sequence. Then, it proceeds with fitness calculation for each horse and iteratively updates the positions of stallions and foals using a combination of strategies, including Lévy flight and mean crossover. The algorithm prioritises finding the

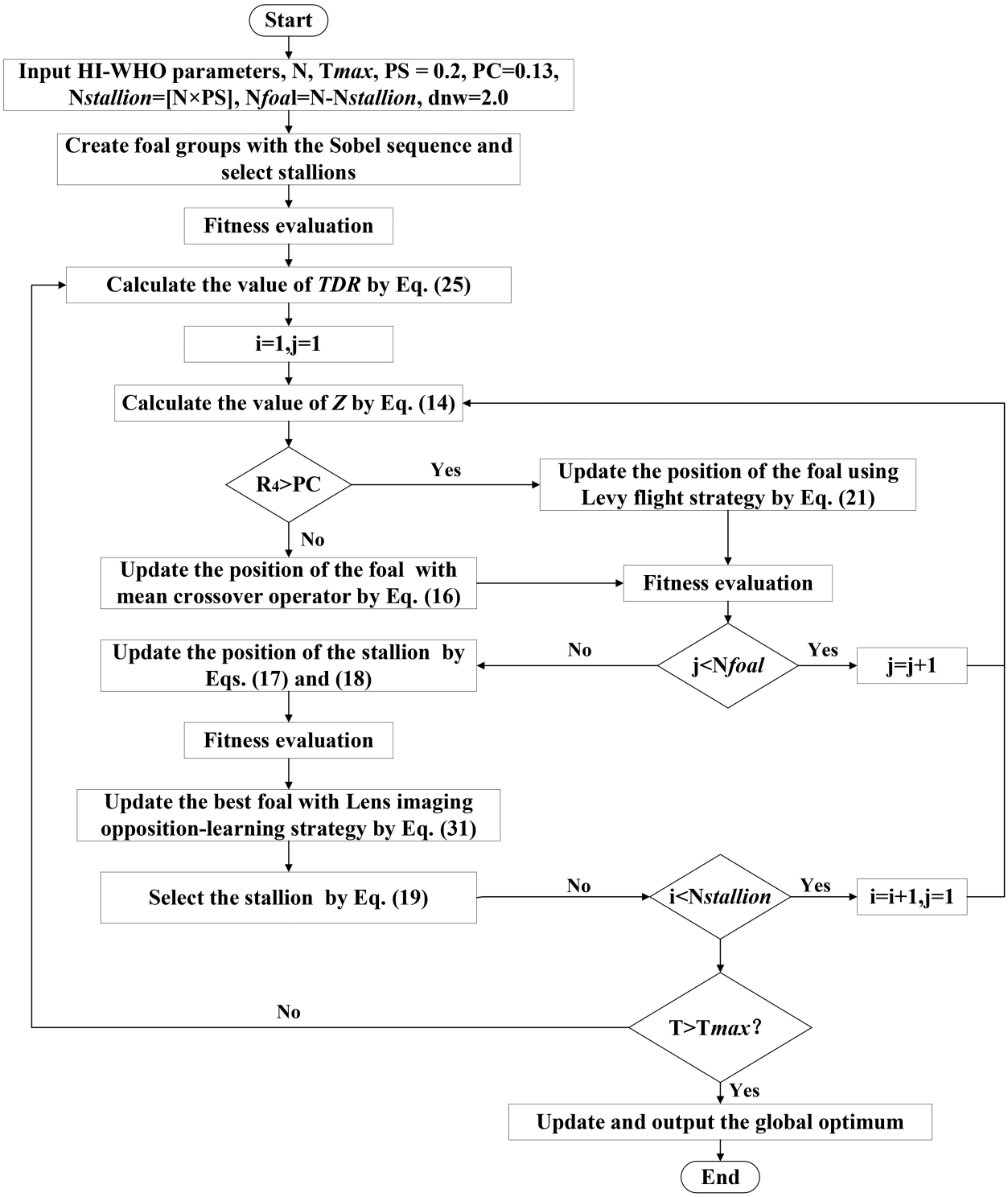

Figure 8. Flowchart of the HI-WHO.

best positions and exchanges positions between foals and stallions as needed. Finally, the algorithm updates and outputs the global optimal solution.

5. Benchmark Function Testing and Result Analysis

This section assesses the performance of HI-WHO with various benchmark functions. We start by introducing the benchmark functions and experimental parameters. Then, the core of the chapter focuses on analysing the results and comparing performance, accuracy, convergence, and stability with different algorithms.

5.1 Benchmark Functions

This paper selected 15 classic benchmark functions from [21]–[23] and 5 CEC2022 benchmark functions from [24] to assess the effectiveness of HI-WHO in addressing global optimisation problems. Functions $F_1 - F_5$ belong

Table 1
Unimodal Benchmark Functions

No.	Function name	Expression	Dimension	Range	Optima
F_1	Sphere	$f_1(x) = \sum_{i=1}^{n} x_i^2$	30/50/100	[−100,100]	0
F_2	Schwefel 2.22	$f_2(x) = \sum_{i=1}^{n} \lvert x_i \rvert + \prod_{i=1}^{n} \lvert x_i \rvert$	30/50/100	[−10,10]	0
F_3	Rosenbrock	$f_3(x) = \sum_{i=1}^{n-1} [100(x_{i+1} - x_i^2)^2 + (x_i - 1)^2]$	30/50/100	[−30,30]	0
F_4	Step	$f_4(x) = \sum_{i=1}^{n} (\lvert x_i + 0.5 \rvert)^2$	30/50/100	[−100,100]	0
F_5	Quartic	$f_5(x) = \sum_{i=1}^{n} i x_i^4 + \text{random}(0, 1)$	30/50/100	[−1.28,1.28]	0

Table 2
Multimodal Benchmark Functions

No.	Function name	Expression	Dimension	Range	Optima
F_6	Schwefel 2.26	$f_6(x) = -\sum_{i=1}^{n} [x_i \sin(\sqrt{\lvert x_i \rvert})]$	30/50/100	[−500,500]	0
F_7	Rastrigin	$f_7(x) = \sum_{i=1}^{n} [x_i^2 - 10\cos(2\pi x_i) + 10]$	30/50/100	[−5.12, 5.12]	0
F_8	Ackley	$f_8(x) = -20\exp(-0.2\sqrt{\frac{1}{n}\sum_{i=1}^{n} x_i^2}) - \exp[\frac{1}{n}\sum_{i=1}^{n} \cos(2\pi x_i)] + 20 + e$	30/50/100	[−32,32]	0
F_9	Griewank	$f_9(x) = \frac{1}{4000}\sum_{i=1}^{n} x_i^2 - \prod_{1}^{n} \cos(\frac{x_i}{\sqrt{i}}) + 1$	30/50/100	[−600,600]	0
F_{10}	Penalized 1.1	$f_{10}(x) = \frac{\pi}{n}\{10\sin^2(\pi y_i) + \sum_{i=1}^{n-1}(y_i - 1)^2 [1 + 10\sin^2(\pi y_{i+1})] + (y_n - 1)^2\} + \sum_{i=1}^{n} u(x_i, 10, 100, 4)$; $y_i = 1 + \frac{1}{4}(x_i + 1)$; $u(x_i, a, k, m) = \begin{cases} k(x_i - a)^m, x_i > a \\ 0, -a \le x_i \le a \\ k(-x_i - a)^m, x_i < -a \end{cases}$	30/50/100	[−50,50]	0

to the unimodal functions, which enable the assessment of exploitation capacity and convergence speed. Functions $F_6 - F_{10}$ represent the multimodal functions, which are utilised to evaluate the global exploration ability. Functions $F_{11} - F_{15}$ are fixed-dimension multipeak functions, allowing for the assessment of stability and the ability to explore in low dimensions. The selected 5 CEC2022 benchmark functions include a unimodal function (F_{16}), two basic functions ($F_{17} - F_{18}$), a hybrid function (F_{19}), and a composite function (F_{20}). The function names, expressions, dimensions, search ranges, and optimal values are provided in Tables 1–4.

5.2 Experimental Parameter Settings

Comparative tests were conducted using six algorithms: the standard WHO [10], the improved WHO (IWHO) [11], the Lévy flight-based improved WHO (IWHOLF) [25], the improved particle swarm optimisation (IPSO) algorithm [26], and the improved sparrow search algorithm (ISSA) [9]. Functions F_1–F_{10} were evaluated across dimensions 30, 50, and 100, and for the CEC2022 test suites, a dimension of 10 was used. These algorithms ran independently on the same machine, employing an Intel(R) Core (TM) i7-8550U CPU @1.8GHz, and 32GB of RAM. MATLAB R2020a was the software utilized. The population size $N = 50$, and the maximum number of iterations $T_{\max} = 1{,}000$. Specific parameters for each algorithm aligned with those defined in the original literature, as summarized in Table 5.

5.3 Analysis of Results and Comparison of Algorithm Performance

5.3.1 Analysis of Optimisation Accuracy

Tables 6 and 7 present the minimum (*Min*), average (*Mean*), and the standard deviation (*Std*) of the results obtained from running each algorithm 50 times. The optimal values for each item are bolded for clarity.

The results in Tables 6 and 7 reveal that HI-WHO performs better than other algorithms in handling unimodal and multimodal problems. Specifically, it achieves optimal values in the unimodal functions F_1 and F_2, as well as the multimodal functions F_7 and F_9. Except

Table 3
Fixed-dimension Multipeak Benchmark Functions

No.	Function name	Expression	Dimension	Range	Optima
F_{11}	Foxholes	$f_{11}(x) = \left[\frac{1}{500} + \sum_{j=1}^{25} \frac{1}{j+\sum_{i=1}^{2}(x_i - a_{ij})^6}\right)\right]^{-1}$	2	[−65.536, 65.536]	1
F_{12}	Kowalik	$f_{12}(x) = \sum_{i=1}^{11}[a_i - \frac{x_1(b_i^2+b_i x_2)}{b_i^2+b_i x_3+x_4}]^2$	4	[−5,5]	0.0003
F_{13}	Branin	$f_{13}(x) = \left(x_2 - \frac{5.1}{4\pi^2}x_1^2 + \frac{5}{\pi}x_1 - 6\right)^2$ $+10\left(1 - \frac{1}{8\pi}\right)\cos x_1 + 10$	2	[−5,10], [0,15]	0.3983
F_{14}	Goldstein price	$f_{14}(x) = [1 + (x_1 + x_2 + 1)^2(19 - 14x_1 + 3x_1^2$ $-14x_2 + 6x_1x_2 + 3x_2^2)]$ $\times[30 + (2x_1 - 3x_2)^2(18 - 32x_1 + 12x_1^2$ $+48x_2 - 36x_1x_2 + 27x_2^2)]$	2	[−2,2]	3
F_{15}	Shekel10	$f_{15}(x) = -\sum_{i=1}^{10}\left[(X - a_i)(X - a_i)^T + c_i\right]^{-1}$	4	[0,10]	−10.5363

Table 4
CEC2022 Benchmark Functions

No.	Function name	Class	Range	Optima
F_{16}	Shifted and full rotated Zakharov function	Unimodal	[−100,100]	300
F_{17}	Shifted and full rotated expanded Scaffer's F6 function	Multimodal	[−100,100]	600
F_{18}	Shifted and full rotated non-continuous Rastrigin's function	Multimodal	[−100,100]	800
F_{19}	Hybrid function 3 ($N = 5$)	Hybrid	[−100,100]	2200
F_{20}	Composite function 4 ($N = 6$)	Composite	[−100,100]	2700

Table 5
Parameter Settings

Algorithm	Parameters
WHO	$PC = 0.13$, $PS = 0.2$
IWHO	$PC = 0.13$, $PS = 0.2$, $PRR = 0.1$, $\omega \in [0.01, 0.99]$
IWHOLF	$PC = 0.13$, $PS = 0.2$
HI-WHO	$PC = 0.13$, $PS = 0.2$, $dnw = 2.0$
IPSO	$c_1 = c_2 = 2$, $w = 1.2$
ISSA	$ST = 0.8$, $PD = 0.3$, $SD = 0.2$

for a few cases in F_3, F_6, and F_{10}, HI-WHO demonstrates significantly superior accuracy and stability across different dimensions. Moreover, HI-WHO outperforms the standard WHO regarding the minimum value, average value, and standard deviation from 50 independent runs. These findings underscore the significant enhancements and effectiveness of the proposed algorithm, indicating that by refining the initial population, HI-WHO benefits from a more extensive search space. Incorporating the Lévy flight strategy amplifies local exploitation capabilities, boosting global optimisation performance. Additionally, integrating the lens imaging opposition-based learning strategy further fortifies the algorithm's capacity to escape local optima.

Table 8 provides a comparative analysis of the performance on fixed-dimensional multimodal functions, which evaluate the capability in balancing exploration and exploitation. The data in the table reveals that all these algorithms approach the optimal values for functions F_{11} to F_{15}. However, HI-WHO consistently outperforms the other algorithms. Notably, for function F_{14}, HI-WHO attains the optimal value for the minimum and average values. This outcome underscores the effective equilibrium the proposed algorithm achieves by introducing dynamic nonlinear adaptive factor, enhancing its global and local search performance.

Table 9 illustrates the results of the six algorithms tackling five intricate global optimisation problems sourced from the CEC2022 test suites. These functions have undergone shifts and rotations, complicating the search for their global optimal values. Solving these functions in lower dimensions effectively evaluates the performance of metaheuristic algorithms [27]. An analysis of the results reveals that, except for function F_{19}, where HI-WHO ranks second in standard deviation (*Std*), surpassed only by the IWHOLF algorithm, HI-WHO consistently delivers the top results across the remaining test cases. The proposed algorithm excels in addressing complex global optimisation problems.

Table 6
Comparison of Optimization Results on Uni-modal and Multimodal Benchmark Test Functions ($F_1 - F_{10}$)

Function	D	HI-WHO			WHO		
		Min	*Mean*	*Std*	*Min*	*Mean*	*Std*
F_1	30	**0.000E+00**	**0.000E+00**	**0.000E+00**	2.242E-141	1.251E-128	6.422E-128
	50	**0.000E+00**	**0.000E+00**	**0.000E+00**	4.221E-128	2.645E-112	1.867E-111
	100	**0.000E+00**	**0.000E+00**	**0.000E+00**	7.171E-123	1.280E-107	7.738E-107
F_2	30	**0.000E+00**	**0.000E+00**	**0.000E+00**	2.138E-77	1.520E-70	4.817E-70
	50	**0.000E+00**	**0.000E+00**	**0.000E+00**	6.849E-71	6.084E-64	2.264E-63
	100	**0.000E+00**	**0.000E+00**	**0.000E+00**	4.293E-68	8.324E-61	4.982E-60
F_3	30	9.711E-12	**1.827E-06**	**5.057E-06**	2.300E+01	2.414E+01	3.676E-01
	50	**6.410E-10**	**2.771E-05**	**6.676E-05**	4.392E+01	4.480E+01	3.548E-01
	100	**7.507E-10**	**8.227E-05**	**2.279E-04**	9.430E+01	9.562E+01	7.276E-01
F_4	30	**1.154E-21**	**1.123E-17**	**2.504E-17**	3.073E-18	3.709E-14	1.370E-13
	50	**8.483E-17**	**8.523E-12**	**2.373E-11**	5.764E-08	2.233E-05	5.495E-05
	100	**8.072E-13**	**1.445E-07**	**8.878E-07**	5.121E-02	5.126E-01	3.145E-01
F_5	30	**9.051E-07**	**3.118E-05**	**2.960E-05**	2.144E-05	3.604E-04	2.439E-04
	50	**3.359E-07**	**3.133E-05**	**3.636E-05**	4.168E-05	2.889E-04	1.898E-04
	100	**1.400E-07**	**3.339E-05**	**3.566E-05**	4.118E-05	3.964E-04	2.668E-04
F_6	30	**−1.257E+04**	**−1.200E+04**	8.956E+02	−1.069E+04	−9.293E+03	5.500E+02
	50	**−2.095E+04**	−1.958E+04	1.905E+03	−1.583E+04	−1.420E+04	7.340E+02
	100	**−4.190E+04**	−3.923E+04	3.742E+03	−2.840E+04	−2.485E+04	1.159E+03
F_7	30	**0.000E+00**	**0.000E+00**	**0.000E+00**	**0.000E+00**	**0.000E+00**	**0.000E+00**
	50	**0.000E+00**	**0.000E+00**	**0.000E+00**	**0.000E+00**	**0.000E+00**	**0.000E+00**
	100	**0.000E+00**	**0.000E+00**	**0.000E+00**	**0.000E+00**	**0.000E+00**	**0.000E+00**
F_8	30	**8.882E--16**	**8.882E-16**	**0.000E+00**	**8.882E-16**	2.522E-15	1.789E-15
	50	**8.882E-16**	**8.882E-16**	**0.000E+00**	**8.882E-16**	2.665E-15	1.794E-15
	100	**8.882E-16**	**8.882E-16**	**0.000E+00**	**8.882E-16**	3.091E-15	1.742E-15
F_9	30	**0.000E+00**	**0.000E+00**	**0.000E+00**	**0.000E+00**	**0.000E+00**	**0.000E+00**
	50	**0.000E+00**	**0.000E+00**	**0.000E+00**	**0.000E+00**	**0.000E+00**	**0.000E+00**
	100	**0.000E+00**	**0.000E+00**	**0.000E+00**	**0.000E+00**	**0.000E+00**	**0.000E+00**
F_{10}	30	3.139E-22	**2.048E-18**	**8.992E-18**	3.497E-20	3.940E-16	1.421E-15
	50	**3.609E-17**	**3.879E-13**	**7.469E-13**	1.564E-10	5.083E-03	1.703E-02
	100	**2.684E-16**	**1.362E-10**	**2.904E-10**	1.606E-04	6.100E-03	8.900E-03

Table 6
Continued

Function	D	IWHO			IWHOLF		
		Min	*Mean*	*Std*	*Min*	*Mean*	*Std*
F_1	30	5.071E-14	5.442E-04	2.618E-03	1.303E-188	8.671E-170	**0.000E+00**
	50	1.358E-15	1.905E-03	5.570E-03	3.046E-187	9.630E-170	**0.000E+00**
	100	3.057E-11	8.104E-03	5.230E-02	7.502E-184	1.103E-165	**0.000E+00**
F_2	30	6.198E-08	4.246E-03	1.260E-02	2.840E-119	2.826E-108	1.458E-107
	50	3.818E-07	1.196E-02	4.103E-02	2.843E-118	9.234E-109	5.723E-108
	100	7.532E-08	1.279E-02	3.747E-02	9.675E-118	2.763E-106	1.371E-105
F_3	30	5.089E-02	2.420E+01	1.002E+01	2.591E+01	2.658E+01	2.891E-01
	50	1.196E-01	4.321E+01	1.514E+01	4.647E+01	4.692E+01	3.807E-01
	100	4.008E-01	8.427E+01	3.340E+01	9.651E+01	9.719E+01	3.593E-01
F_4	30	7.267E-03	1.551E+00	1.261E+00	1.274E-03	8.619E-03	3.318E-02
	50	8.461E-03	3.716E+00	2.738E+00	1.777E-02	5.597E-02	4.788E-02
	100	1.285E-01	6.526E+00	5.987E+00	2.152E-01	5.535E-01	2.032E-01
F_5	30	4.911E-04	4.184E-03	4.255E-03	1.590E-05	1.019E-03	1.022E-03
	50	6.996E-05	6.749E-03	6.542E-03	1.231E-05	9.384E-04	1.309E-03
	100	2.352E-05	5.698E-03	6.459E-03	2.303E-05	1.106E-03	1.394E-03
F_6	30	−1.254E+04	−1.047E+04	1.654E+03	−1.257E+04	−1.164E+04	1.369E+03
	50	**−2.095E+04**	−1.780E+04	2.408E+03	**−2.095E+04**	**−1.996E+04**	1.747E+03
	100	−4.186E+04	−3.456E+04	5.886E+03	**−4.190E+04**	**−3.943E+04**	3.621E+03
F_7	30	**0.000E+00**	1.608E-04	4.199E-04	**0.000E+00**	**0.000E+00**	**0.000E+00**
	50	**0.000E+00**	5.588E-03	2.721E-02	**0.000E+00**	**0.000E+00**	**0.000E+00**
	100	**0.000E+00**	1.537E-02	9.557E-02	**0.000E+00**	1.364E-14	5.455E-14
F_8	30	2.789E-10	3.315E-03	1.455E-02	**8.882E-16**	4.512E-15	2.091E-15
	50	1.143E-09	3.490E-03	8.306E-03	**8.882E-16**	4.228E-15	2.425E-15
	100	1.433E-09	7.676E-03	2.000E-02	**8.882E-16**	4.299E-15	2.584E-15
F_9	30	9.992E-16	1.077E-02	7.116E-02	**0.000E+00**	1.848E-03	9.154E-03
	50	1.221E-14	1.814E-03	7.979E-03	**0.000E+00**	1.063E-03	7.513E-03
	100	**0.000E+00**	2.404E-02	1.623E-01	**0.000E+00**	4.623E-03	2.302E-02
F_{10}	30	1.273E-04	5.451E-02	9.813E-02	1.514E-04	1.870E-03	3.795E-03
	50	1.029E-04	6.212E-02	8.759E-02	7.320E-04	2.666E-03	2.552E-03
	100	1.941E-04	9.144E-02	1.572E-01	1.708E-03	6.738E-03	9.501E-03

Table 7
Comparison of Optimization Results on Uni-modal and Multimodal Benchmark Test Functions ($F_1 - F_{10}$)

Function	D	IPSO			ISSA		
		Min	*Mean*	*Std*	*Min*	*Mean*	*Std*
F_1	30	4.422E-26	6.000E-02	2.399E-01	**0.000E+00**	2.341E-176	**0.000E+00**
	50	1.182E-09	5.801E-01	6.728E-01	**0.000E+00**	5.307E-171	**0.000E+00**
	100	1.119E+00	4.340E+00	1.616E+00	**0.000E+00**	2.790E-164	**0.000E+00**
F_2	30	1.857E-10	8.002E-01	8.329E-01	**0.000E+00**	6.157E-90	3.538E-89
	50	1.940E-02	2.983E+00	1.460E+00	**0.000E+00**	8.266E-89	4.918E-88
	100	6.934E+00	1.098E+01	2.555E+00	**0.000E+00**	2.904E-87	1.943E-86
F_3	30	**0.000E+00**	7.294E+01	6.052E+01	1.530E-06	4.030E+00	1.006E+01
	50	4.000E+00	2.153E+02	1.106E+02	2.881E-05	1.068E+01	2.029E+01
	100	3.963E+02	6.809E+02	1.511E+02	9.196E-05	7.883E+00	2.684E+01
F_4	30	2.500E-01	1.830E+00	6.897E-01	1.130E-08	3.530E-06	4.220E-06
	50	2.000E+00	4.770E+00	1.444E+00	2.049E-07	1.019E-05	1.440E-05
	100	8.751E+00	1.442E+01	2.738E+00	1.399E-07	3.758E-05	6.725E-05
F_5	30	2.684E-02	8.306E-01	1.136E+00	1.018E-05	3.231E-04	2.693E-04
	50	3.330E-01	6.966E+00	6.791E+00	2.072E-05	3.315E-04	3.014E-04
	100	1.503E+01	9.108E+01	4.320E+01	5.624E-06	3.655E-04	4.008E-04
F_6	30	−2.524E+01	−2.343E+01	**1.515E+00**	−1.013E+04	−8.402E+03	6.018E+02
	50	−4.207E+01	−3.578E+01	**2.999E+00**	−1.498E+04	−1.325E+04	8.747E+02
	100	−7.405E+01	−5.874E+01	**6.141E+00**	−2.963E+04	−2.534E+04	1.349E+03
F_7	30	2.600E+01	2.790E+01	7.357E-01	**0.000E+00**	**0.000E+00**	**0.000E+00**
	50	4.599E+01	4.806E+01	8.184E-01	**0.000E+00**	**0.000E+00**	**0.000E+00**
	100	9.600E+01	9.800E+01	9.252E-01	**0.000E+00**	**0.000E+00**	**0.000E+00**
F_8	30	1.377E+00	2.055E+00	2.983E-01	**8.882E-16**	**8.882E-16**	**0.000E+00**
	50	1.857E+00	2.434E+00	2.129E-01	**8.882E-16**	**8.882E-16**	**0.000E+00**
	100	2.237E+00	2.545E+00	1.441E-01	**8.882E-16**	**8.882E-16**	**0.000E+00**
F_9	30	**0.000E+00**	2.585E-02	2.496E-02	**0.000E+00**	**0.000E+00**	**0.000E+00**
	50	1.272E-02	6.454E-02	2.863E-02	**0.000E+00**	**0.000E+00**	**0.000E+00**
	100	7.949E-02	1.356E-01	3.130E-02	**0.000E+00**	**0.000E+00**	**0.000E+00**
F_{10}	30	**1.571E-32**	3.194E-02	2.813E-02	1.366E-08	3.141E-06	1.032E-05
	50	1.571E-02	7.477E-02	3.003E-02	1.058E-08	2.284E-06	4.881E-06
	100	9.425E-02	1.660E-01	5.522E-02	2.187E-09	1.249E-03	6.158E-03

5.3.2 Analysis of Convergence Accuracy and Algorithm Stability

For a more intuitive assessment of the performance, Fig. 9 depicts the convergence curves of the six algorithms while tackling the complex benchmark functions F_1 to F_{10} in D = 100 dimension and the fixed-dimensional functions F_{11} to F_{15}.

The observed convergence curves in Fig. 9 indicate the superior performance of HI-WHO over the other algorithms. It exhibits faster convergence, reduced instances of local optima entrapment, and enhanced optimisation accuracy and capability. For high-dimensional unimodal and multimodal problems (F_3, F_6, F_7, F_8, and F_9), HI-WHO consistently achieves convergence to the optimal value with the fewest iterations and showcases superior optimisation ability. Additionally, in the case of solving problems (F_1, F_2, F_4, F_5, F_8, and F_{10}), HI-WHO consistently delivers higher optimisation accuracy. When dealing with fixed-dimensional multimodal problems, HI-WHO, and other algorithms closely approach the theoretical optimum. However, HI-WHO distinguishes

Table 8
Comparison of Optimization Results on Fixed-dimensional Benchmark Test Functions ($F_{11} - F_{15}$)

Function	D	HI-WHO			WHO		
		Min	*Mean*	*Std*	*Min*	*Mean*	*Std*
F_{11}	2	**9.980E-01**	**9.980E-01**	**3.351E-10**	**9.980E-01**	1.236E+00	7.872E-01
F_{12}	4	**3.075E-04**	**3.075E-04**	**1.298E-17**	**3.075E-04**	1.435E-03	3.924E-03
F_{13}	2	**3.979E-01**	**3.979E-01**	**3.365E-16**	**3.979E-01**	**3.979E-01**	1.286-06
F_{14}	2	**3.000E+00**	**3.000E+00**	**1.651E-15**	**3.000E+00**	**3.000E+00**	3.591E-05
F_{15}	4	**−1.054E+01**	**−1.043E+01**	**7.648E-01**	**−1.054E+01**	−9.137E+00	2.848E+00
Function	D	IWHO			IWHOLF		
		Min	*Mean*	*Std*	*Min*	*Mean*	*Std*
F_{11}	2	**9.980E-01**	3.923E+00	3.589E+00	**9.980E-01**	1.511E+00	1.510E+00
F_{12}	4	3.323E-04	1.192E-03	1.694E-03	3.077E-04	5.845E-04	2.837E-04
F_{13}	2	**3.979E-01**	**3.979E-01**	6.395E-08	**3.979E-01**	**3.979E-01**	2.075E-07
F_{14}	2	**3.000E+00**	**3.000E+00**	3.579E-15	**3.000E+00**	**3.000E+00**	2.243E-15
F_{15}	4	**−1.054E+01**	−8.807E+00	2.953E+00	**−1.054E+01**	−8.833E+00	2.963E+00
Function	D	IPSO			ISSA		
		Min	*Mean*	*Std*	*Min*	*Mean*	*Std*
F_{11}	2	1.267E+01	1.267E+01	1.197E-13	**9.980E-01**	3.571E+00	4.644E+00
F_{12}	4	3.075E-04	5.605E-04	9.328E-04	1.674E-03	1.675E-03	4.161E-07
F_{13}	2	2.770E+01	2.770E+01	3.589E-14	**3.979E-01**	5.051E-01	1.928E-01
F_{14}	2	**3.000E+00**	**3.000E+00**	2.832E-06	**3.000E+00**	**3.000E+00**	5.344E-12
F_{15}	4	−5.129E+00	−5.129E+00	2.692E-15	**−1.054E+01**	−9.021E+00	2.452E+00

itself by demonstrating the highest level of stability in these scenarios, rapidly converging to the theoretical optimum values in optimising functions F_{11} to F_{15}.

Figure 10 illustrates the dynamic changes in exploration and exploitation percentages of HI-WHO during the CEC2022 benchmark functions optimisation process. The enhancement strategies can be effectively evaluated by conducting dimensional diversity tests and quantifying exploration and exploitation percentages at each iteration [28], [29]. The figures show that HI-WHO successfully bolsters its global exploration and local exploitation capabilities by optimising the initial population distribution and integrating dynamic nonlinear adaptive factor.

6. Application of HI-WHO in Robot Path Planning

This section conducts simulation experiments in simple and complex grid map environments to validate the HI-WHO's feasibility and effectiveness for robot path planning. The comparative analysis includes the improved PSO algorithm [27], ISSA [9], the standard WHO, and the enhanced HI-WHO. Under consistent conditions, all algorithms had a population size (N) of 30 and a maximum of 200 iterations ($T_{\max}$). The parameter settings for the comparative algorithms are presented in Table 5.

6.1 Robot Path Planning in Simple Environment

The experiment in the simple environment is conducted on a grid map with its size limited in 30×30. The robot starts from the circular at coordinate (0.5,0.5) and moves towards the target point represented by the pentagram at coordinate (29.5,29.5). After 30 repeated experiments, the paths are compared in Fig. 11 (a), and the corresponding fitness curves are shown in Fig. 11 (b). The worst, best, average value, standard deviation, and turn times are summarised, as presented in Table 10.

From Figs. 11(a) and (b), it can be observed that all algorithms avoid obstacles and complete the path planning from the start point to the target point. The improved PSO algorithm converges to a fitness value of 43.24 after 49 iterations, the ISSA converges to a fitness value of 43.70 after 20 iterations, the standard WHO converges to a fitness value of 42.08 after 49 iterations, and the improved HI-WHO converges to a fitness value of 41.65 after 39 iterations. The fitness value reflects path length since no planned paths intersect with obstacles,

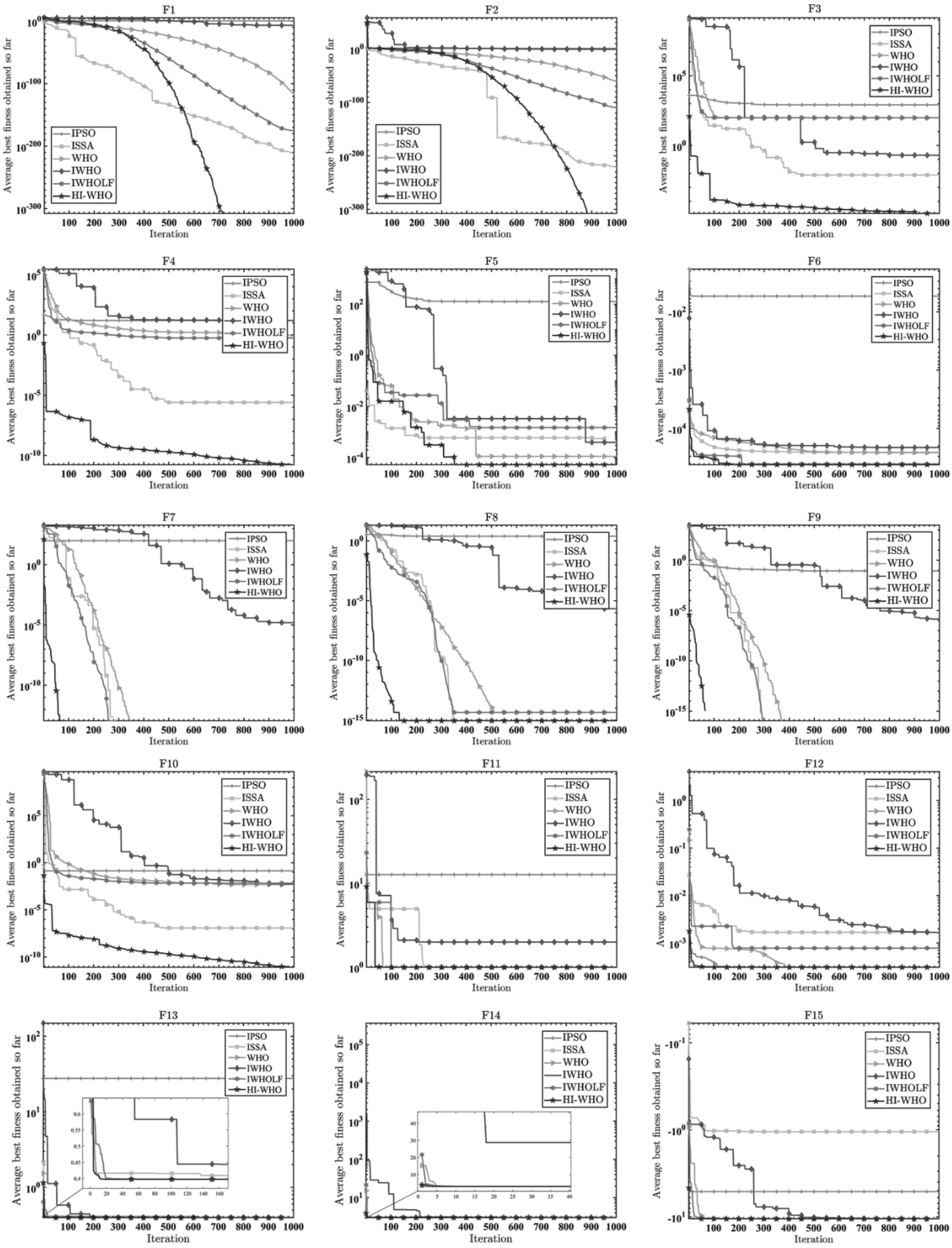

Figure 9. Convergence curves of six algorithms on benchmark test functions F_1 to F_{15}.

Table 9
Comparison of Optimization Results on CEC2022 Benchmark Test Functions (F_{16} - F_{20}, D=10)

Function	HI-WHO			WHO		
	Min	*Mean*	*Std*	*Min*	*Mean*	*Std*
F_{16}	**3.000E+02**	**3.000E+02**	**1.087E-13**	**3.000E+02**	3.006E+02	1.145E+02
F_{17}	**6.000E+02**	**6.003E+02**	**1.449E+00**	6.174E+02	6.158E+02	4.735E+00
F_{18}	**8.040E+02**	**8.108E+02**	**4.516E+00**	8.300E+02	8.445E+02	6.871E+00
F_{19}	**2.200E+03**	**2.216E+03**	8.798E+00	2.234E+03	2.313E+03	6.479E+01
F_{20}	**2.859E+03**	**2.865E+03**	**2.603E+00**	2.903E+03	2.904E+03	6.606E-01
Function	IWHO			IWHOLF		
	Min	*Mean*	*Std*	*Min*	*Mean*	*Std*
F_{16}	**3.000E+02**	3.004E+02	1.279E-04	**3.000E+02**	3.021E+02	2.042E-10
F_{17}	6.144E+02	6.152E+02	1.187E+01	6.102E+02	6.117E+02	1.216E+01
F_{18}	8.167E+02	8.407E+02	1.181E+01	8.091E+02	8.351E+02	1.459E+01
F_{19}	2.224E+03	2.239E+03	2.356E+01	2.216E+03	2.230E+03	**5.211E+00**
F_{20}	2.869E+03	2.897E+03	2.919E+01	2.864E+03	2.884E+03	2.395E+01
Function	IPSO			ISSA		
	Min	*Mean*	*Std*	*Min*	*Mean*	*Std*
F_{16}	3.065E+02	3.067E+02	4.624E-12	**3.000E+02**	3.071E+02	2.042E+03
F_{17}	6.187E+02	6.193E+02	1.963E+01	6.186E+02	6.142E+02	1.420E+01
F_{18}	8.956E+02	8.956E+02	1.345E+01	8.314E+02	8.562E+02	1.500E+01
F_{19}	2.576E+03	2.576E+03	2.280E+01	2.226E+03	2.237E+03	1.529E+01
F_{20}	2.919E+03	2.920E+03	3.567E+00	2.879E+03	2.962E+03	5.707E+01

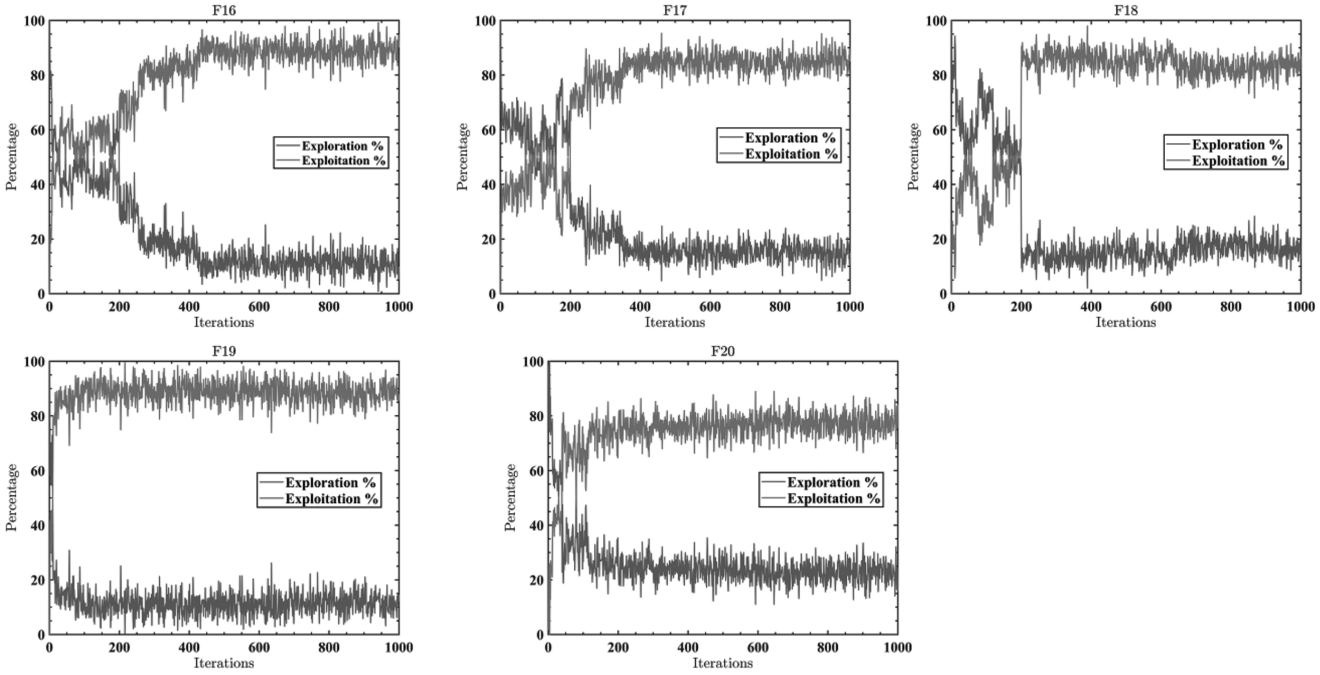

Figure 10. Exploration and exploitation of HI-WHO on CEC2022 benchmark test functions.

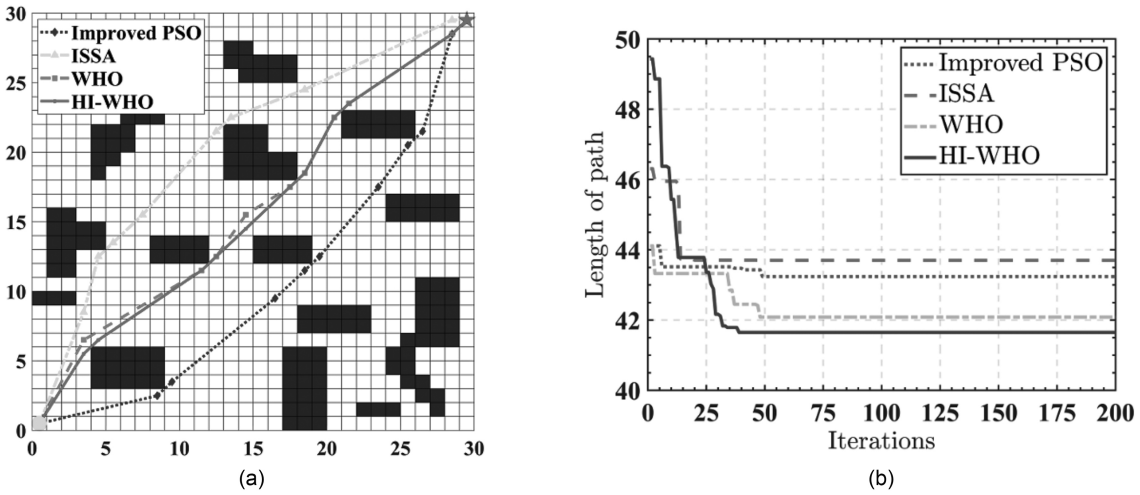

Figure 11. Optimal paths and convergence curves of improved PSO, ISSA, WHO, and HI-WHO.

Table 10
Experimental Results in Simple Environment

Algorithm	Worst	Best	Average	Std	Turn times
Improved PSO	46.87	43.24	45.62	0.46	10
ISSA	48.17	43.70	47.49	0.62	9
WHO	44.26	42.08	43.74	0.28	10
HI-WHO	42.14	41.65	41.36	0.12	8

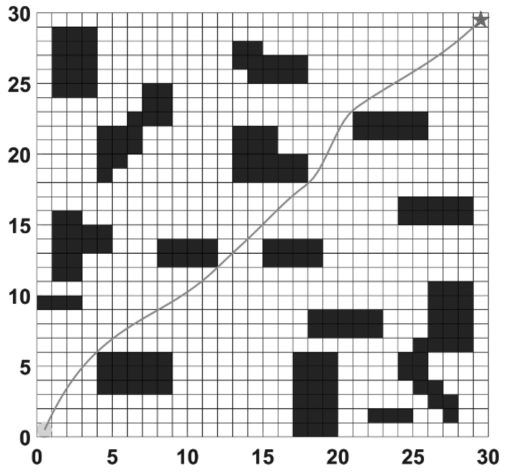

Figure 12. Effect of path smoothing using B-spline curve.

as per (3). Consequently, in a comparative analysis of the path planning results, HI-WHO achieves the optimal path length. Compared to the standard WHO, HI-WHO generates a shorter path, thereby reducing the number of iterations by 20%.

From the results in Table 10, it can be observed that in the 30 repeated path planning experiments, HI-WHO has the lowest average path length and the most minor standard deviation. The paths generated by HI-WHO exhibit less variation between each planning iteration, indicating higher stability than other algorithms.

Table 11
Experimental Results in Realistically Abstracted Grid Map Environment

Algorithm	Worst	Best	Average	Std	Turn times
Improved PSO	80.72	76.32	78.76	0.69	10
ISSA	78.23	75.40	77.12	0.73	10
WHO	76.14	74.71	75.68	0.48	11
HI-WHO	72.54	72.01	72.27	0.16	8

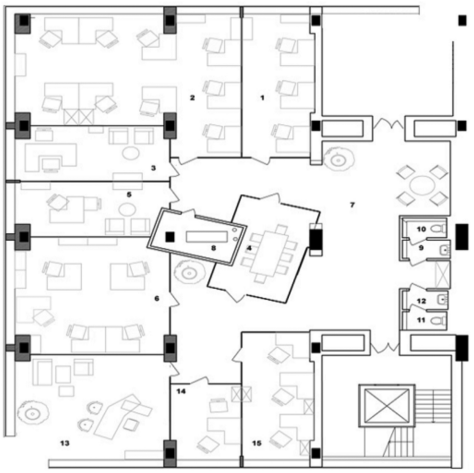

Figure 13. Floor plan of a real building structure.

Figure 12 illustrates the effect of applying B-spline curve smoothing the path generated by HI-WHO. The obtained path exhibits smoother changes in the turning angles, effectively avoiding sharp turns or jittering, thereby improving the efficiency and stability of the robot's movements.

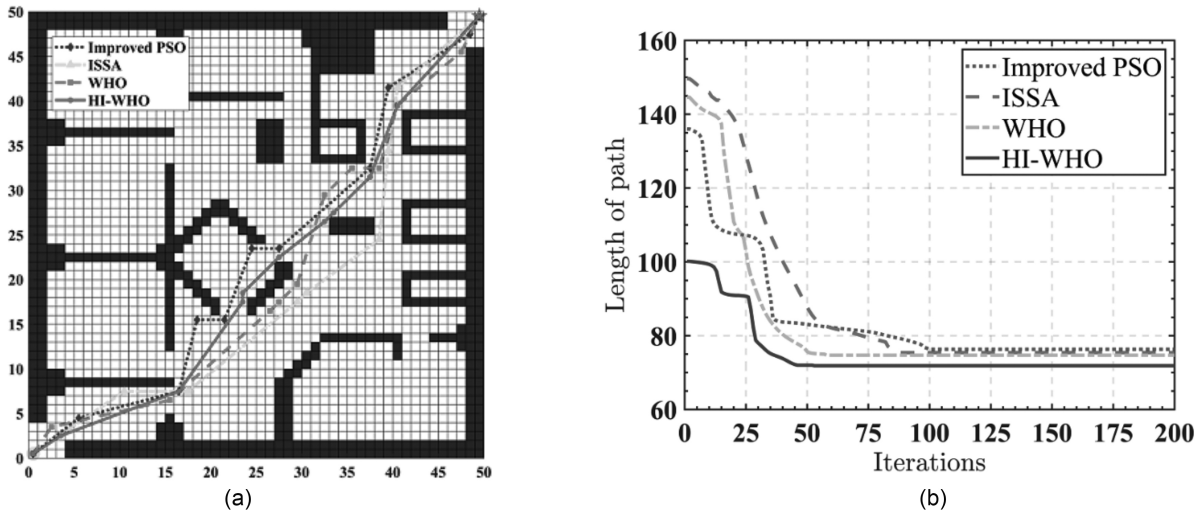

Figure 14. Optimal paths generated by improved PSO, ISSA, WHO, and HI-WHO.

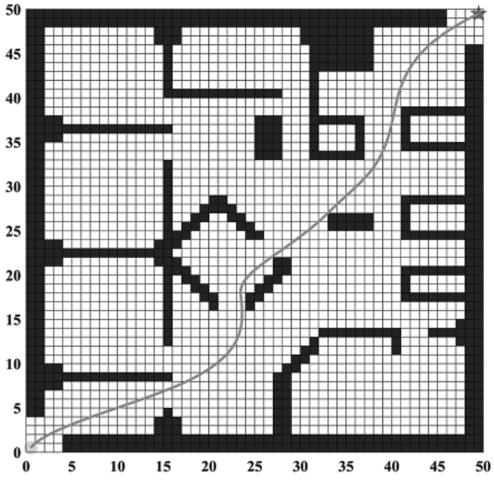

Figure 15. Effect of path smoothing using B-spline curve.

6.2 Robot Path Planning in Realistically Abstracted Grid Map Environment

We carried out path planning experiments on a natural building floor structure employing a grid-based environment representation, as depicted in Fig. 13, to further validate the practicality and efficacy of the enhanced HI-WHO in addressing real-world path planning challenges. The results are shown in Figs. 14(a) and (b). Similarly, four algorithms were independently tested for 30 trials. The worst, best, average value, standard deviation, and number of turns for each algorithm are presented in Table 11.

Figures 14(a) and (b) reveal that HI-WHO attains the most favourable results among the four algorithms. Specifically, the improved PSO algorithm converges to the optimal value of 76.32 after 100 iterations, ISSA reaches 75.40 in 87 iterations, the standard WHO achieves 74.71 in 58 iterations, and the improved HI-WHO converges to 72.01 after only 46 iterations. Compared to the standard WHO, HI-WHO reduces the number of iterations by 14%. Furthermore, the path generated by HI-WHO exhibits smaller turning angles and better performance than the other three methods.

The results in Table 11 demonstrate that HI-WHO outperforms the other three algorithms regarding the path length and turn times, which indicates that the improved algorithm has the best stability. The effectiveness of HI-WHO can be further illustrated by the smoothed path obtained through the cubic B-spline curve, as shown in Fig. 15. In summary, the enhanced HI-WHO consistently achieves the shortest path and outperforms other algorithms, meeting the demands of global path planning for mobile robots in complex environments.

7. Conclusion and Future Works

This work introduces an enhanced WHO (HI-WHO) with hybrid strategies, aiming to augment the standard WHO and extend its applicability in robot path planning. The proposed algorithm addresses limitations by incorporating Sobol sequences for population initialisation, integrating Lévy flight, dynamic self-adaptive factor, and lens imaging opposition-based learning. These modifications enhance population diversity and balance global exploration and local exploitation. Simulated experiments indicate that HI-WHO achieves faster convergence, with iterations decreasing by 20% and 14% in the respective environments, demonstrating superior performance by producing smooth paths via cubic B-spline curves that fulfil the requirements of global path planning and robot motion control.

Nevertheless, HI-WHO does exhibit limitations, such as encountering local optima when dealing with specific functions in unimodal and multimodal problems (*e.g.*, F_3, F_6, and F_{10}). Additionally, it requires improvements for solving CEC2022 benchmark suites. Our future efforts will aim to refine HI-WHO's performance, with a particular focus on bolstering stability and adaptability in tackling challenges, including multi-robot path planning, dynamic obstacles, and other complex real-world scenarios.

References

[1] N.A. Houacine and H. Drias, When robots contribute to eradicate the COVID-19 spread in a context of containment, *Progress in Artificial Intelligence, 10*(4), 2021, 391–416.

[2] Z. Liu, D. Zhu, C. Liu, and S.X. Yang, A novel path planning algorithm of AUV with model predictive control, *International Journal of Robotics and Automation, 37*(6), 2022, 460–467.

[3] C. Ntakolia, S. Moustakidis, and A. Siouras, Autonomous path planning with obstacle avoidance for smart assistive systems, *Expert Systems with Applications, 213*, 2023, 119049.

[4] L. Sun, Z. Fu, F. Tao, P. Si, S. Song, and C. Sun, APF-bug-based intelligent path planning for autonomous vehicle with high precision in complex environment, I*nternational Journal of Robotics and Automation, 38*(6), 2023, 277–283.

[5] M.N.A. Wahab, S. Nefti-Meziani, and A. Atyabi, A comparative review on mobile robot path planning: Classical or meta-heuristic methods? *Annual Reviews in Control, 50*, 2020, 233–252.

[6] L. Xu, M. Cao, and B. Song, A new approach to smooth path planning of mobile robot based on quartic Bezier transition curve and improved PSO algorithm, *Neurocomputing, 473*, 2022, 98–106.

[7] S. Kumar and A. Sikander, Optimum mobile robot path planning using improved artificial bee colony algorithm and evolutionary programming, *Arabian Journal for Science and Engineering, 47*(3), 2022, 3519–3539.

[8] M. Alweshah, M. Almiani, N. Almansour, S. Al Khalaileh, H. Aldabbas, W. Alomoush, and A. Alshareef, Vehicle routing problems based on Harris Hawks optimization, *Journal of Big Data*, *9*(1), 2022, 42.

[9] G. Zhang and E. Zhang, An improved sparrow search based intelligent navigational algorithm for local path planning of mobile robot, *Journal of Ambient Intelligence and Humanized Computing, 14*, 2023, 14111–14123.

[10] I. Naruei and F. Keynia, Wild horse optimizer: A new meta-heuristic algorithm for solving engineering optimization problems, *Engineering with Computers, 38*(4), 2022, 3025–3056.

[11] R. Zheng, A.G. Hussien, H.-M. Jia, L. Abualigah, S. Wang, and D. Wu, An improved wild horse optimizer for solving optimization problems, *Mathematics, 10*(8), 2022, 1311.

[12] E. García, J.R. Villar, Q. Tan, J. Sedano, and C. Chira, An efficient multi-robot path planning solution using A* and coevolutionary algorithms, *Integrated Computer-Aided Engineering, 30*(1), 2023, 41–52.

[13] T. Liu, J. Li, S.X. Yang, Z. Gong, Z, Liu, H. Zhong, and Q. Fu, Optimal coverage path planning for tractors in hilly areas based on energy consumption model, *International Journal of Robotics and Automation, 38*(6), 2023, 20–31.

[14] L. Wu, X. Huang, J. Cui, C. Liu, and W. Xiao, Modified adaptive ant colony optimization algorithm and its application for solving path planning of mobile robot, *Expert Systems with Applications, 215*, 2023, 119410.

[15] W. Hou, Z. Xiong, C. Wang, and H. Chen, Enhanced ant colony algorithm with communication mechanism for mobile robot path planning, *Robotics and Autonomous Systems, 148*, 2022, 103949.

[16] L. Wang and Y. Guo, Speed adaptive robot trajectory generation based on derivative property of B-Spline curve, *IEEE Robotics and Automation Letters, 8*(4), 2023, 1905–1911.

[17] J. Zhao and X. Luo, Three-dimensional path planning for unmanned aerial vehicle (UAV) based on improved mayfly algorithm, *Proc. 2022 IEEE International Conf. on Unmanned Systems (ICUS).* IEEE, Guangzhou, China, 2022, 32–37.

[18] S. Joe and F.Y. Kuo, Remark on algorithm 659: Implementing Sobol's quasirandom sequence generator, *ACM Transactions on Mathematical Software, 29*(1), 2003, 49–57.

[19] A.H. Gandomi, X.-S. Yang, and A.H. Alavi, Cuckoo search algorithm: A metaheuristic approach to solve structural optimization problems, *Engineering with Computers, 29*(1), 2013, 17–35.

[20] Q. Bo, W. Cheng, and M. Khishe, Evolving chimp optimization algorithm by weighted opposition-based technique and greedy search for multimodal engineering problems, *Applied Soft Computing*, *132,* 2023, 109869.

[21] Y. Shen, C. Zhang, F. Soleimanian Gharehchopogh, and S. Mirjalili, An improved whale optimization algorithm based on multi-population evolution for global optimization and engineering design problems, *Expert Systems with Applications, 215*, 2023, 119269.

[22] S. Zhao, T. Zhang, S. Ma, and M. Wang, Sea-horse optimizer: A novel nature-inspired meta-heuristic for global optimization problems, *Applied Intelligence, 53*(10), 2023, 11833–11860.

[23] G. Hu, J. Wang, Y. Li, M. Yang, and J. Zheng, An enhanced hybrid seagull optimization algorithm with its application in engineering optimization, *Engineering with Computers, 39*(2), 2023, 1653–1696.

[24] M. Abdel-Basset, R. Mohamed, K.M. Sallam, and R.K. Chakrabortty, Light spectrum optimizer: A novel physics-inspired metaheuristic optimization algorithm, *Mathematics, 10*(19), 2022, 3466.

[25] G. Saravanan, S. Neelakandan, P. Ezhumalai, and S. Maurya, Improved wild horse optimization with Lévy flight algorithm for effective task scheduling in cloud computing, *Journal of Cloud Computing, 12*(1), 2023, 24.

[26] B. Song, Z. Wang, and L. Zou, An improved PSO algorithm for smooth path planning of mobile robots using continuous high-degree Bezier curve, *Applied Soft Computing, 100*, 2021, 106960.

[27] W. Xu, R. Zhang, and L. Chen, An improved crow search algorithm based on oppositional forgetting learning, *Applied Intelligence, 52*(7), 2022, 7905–7921.

[28] K. Hussain, M.N.M. Salleh, S. Cheng, and Y. Shi, On the exploration and exploitation in popular swarm-based metaheuristic algorithms, *Neural Computing and Applications, 31*(11), 2019, 7665–7683.

[29] B. Morales-Castañeda, D. Zaldívar, E. Cuevas, F. Fausto, and A. Rodríguez, A better balance in metaheuristic algorithms: Does it exist? *Swarm and Evolutionary Computation, 54*, 2020, 100671.

Biographies

Juntao Zhao received the B.E. degree in electrical engineering and automation from Hebei University of Technology, China, in 2013, and the M.Eng. degree in control engineering from China University of Geosciences Beijing, China, in 2021. He is currently pursuing the doctoral degree with Northeastern University, Shenyang, China. He is also a member of laboratory EPROAD, UPJV, Amiens, France, from 2022. His major research interests include the application of intelligent algorithms, trajectory online optimisation, combinatorial optimisation, and reinforcement learning.

Xiaochuan Luo received the M.Eng. and Ph.D. degrees from Harbin Institute of Technology, Harbin, China, in 1999 and 2002, respectively. From 2002 to 2004, he held a postdoctoral position with the University of Technology of Troyes, Troyes, France. He is currently a Professor with Northeastern University, Shenyang, China. He was selected into the 2008 Ministry of Educations New Century Excellent Talents Support Program and the Million Talents Project in Liaoning Province, in 2009.

His current research interests include modelling and optimisation of processing industry manufacturing systems, production planning and scheduling, and optimisation methods.

Yong Li received the B.E. degree in new energy science and engineering from Xuzhou University of Technology, Xuzhou, China, in 2021, and he is currently pursuing the M.Sc. degree with the College of Information Science and Engineering, Northeastern University, Shenyang, China.

His main research interests include control theory, path optimisation, and intelligent algorithms.